

Surface defect identification using Bayesian filtering on a 3D mesh

Matteo Dalle Vedove^{1,2}, Matteo Bonetto¹, Edoardo Lamon^{3,4}, Luigi Palopoli³,
Matteo Saveriano¹, Daniele Fontanelli¹

Abstract

This paper presents a CAD-based approach for automated surface defect detection. We leverage the a-priori knowledge embedded in a CAD model and integrate it with point cloud data acquired from commercially available stereo and depth cameras. The proposed method first transforms the CAD model into a high-density polygonal mesh, where each vertex represents a state variable in 3D space. Subsequently, a weighted least squares algorithm is employed to iteratively estimate the state of the scanned workpiece based on the captured point cloud measurements. This framework offers the potential to incorporate information from diverse sensors into the CAD domain, facilitating a more comprehensive analysis. Preliminary results demonstrate promising performance, with the algorithm achieving convergence to a sub-millimeter standard deviation in the region of interest using only approximately 50 point cloud samples. This highlights the potential of utilising commercially available stereo cameras for high-precision quality control applications.

1 Introduction

Industry 4.0 relies on the circular dependency between the data collected from the process and their exploitation to adapt and improve the production rate and variety [1]. In this context, automatic defect detection in industrial production and assembly lines is paramount for delivering products that match the continuously increasing levels of quality requirements. A paradigmatic example in the automotive industry is the identification of small defects on metallic surfaces that are the results of faulty welding operations (weld splatters) or other mechanical processes (e.g., dents during the press operation).

According to current industrial practices, the detection of this type of anomalies is performed by human operators, who are specially trained to identify tiny defects in short amounts of time, dictated by the requirements of the production process [2]. In the automotive industry, the takt time, i.e., the time allotted to scan a whole car body surface, is usually in the order of some minutes. At the same time, the task is repetitive and not particularly engaging, hence it appears convenient to involve also robotic operators in some of the steps required in the product quality checks and rework. While it is possible to exploit advanced predictive quality model to speed up the process [3], still the task is non-trivial and presents challenging complexity especially in the defect detection phase. Promising results come from deflectometry, an optical-based method which measures the deformation patterns of structured light [4, 5, 6]. However, a proper application of deflectometry in this context requires a high reflectance of the inspected surface [7]. The direct implication of this requirement in the automotive industry is that vehicles can be inspected with this method only after the painting process. Nevertheless, detecting a defect too late in the process comes with very high reworking costs, which are difficult to accept considering that most of these defects could be revealed right after weld and assembly processes, during the so-called body-in-white phase.

¹Department of Industrial Engineering, Università di Trento, Trento, Italy. matteo.dallevedove@unitn.it

²DRIM, Ph.D. of national interest in Robotics and Intelligent Machines.

³Department of Information Engineering and Computer Science, Università di Trento, Trento, Italy.

⁴Human-Robot Interfaces and Interaction, Istituto Italiano di Tecnologia, Genoa, Italy.

A different approach is to detect defects from images leveraging machine learning methods. Such methods have been extensively investigated in the literature [8, 9, 10], with deep-learning being predominant in recent years [11, 12, 13, 14, 15]. Leveraging high quality images in a heavily structured environment, vision systems proved to be effective, with detection accuracy that can exceed 95% for some specific datasets. The main limitation of these techniques, however, resides in the fact that, to properly train classifiers, big datasets are required and, therefore, human labour to manually label all the possible defects is strictly needed. In addition, they still lack of generalisation capabilities, hence, in case of changes in the production line or for new products, new labelled data is required. Even though unsupervised learning methods overcome this problem by autonomously learning patterns from the data, they are still not mature nor effective enough due to the low accuracy they usually provide [16]. On the other hand, a rich source of information that is always available is the CAD model of the workpiece. This data is mainly used in geometric inspection [17, 18] to assess whether components comply, or not, with the tolerances specified in the CAD model, but little research focused on the exploitation of 3D models to determine surface imperfections [19].

In this paper, we address the surface defect detection problem by combining the a-priori CAD model knowledge with several point-cloud measurements acquired through commercially available stereo cameras. In our method, the CAD drawing is first translated into a high-density polygonal mesh, assigning a degree-of-freedom (a state variable) to each mesh vertex. Based on this representation, we use a weighted least squares to recursively estimate the state of the scanned workpiece. Additionally, this enables the embedding in the CAD domain of information potentially coming from multiple kind of sensors. Preliminary results shows that, with approximately 50 point-cloud samples, the algorithm converges to a state with sub-millimetric standard deviation in the region of interest, effectively showing the potential of commercial stereo and depth cameras in the context of quality inspection.

This paper is organised like this. Sec. 2 reports some background knowledge and reports the proposed algorithm description, while Sec. 3 report the experimental setup and the results obtained. Finally, in Sec. 4, we summarise our work and highlight future works.

2 CAD-based Defect Detection Algorithm

The solution for defect detection here presented builds upon the data acquired from a stereo camera and the prior CAD description of the component to check, whose availability is a customary assumption for production lines. Therefore, this section at first presents the models of the adopted instruments and of the assumed prior data, then we describe how those information are optimally fused together using Bayesian filtering techniques.

2.1 CAD Model

The main goal of the algorithm proposed in this paper is to match the point cloud collected from the sensors with the 3D model of the workpiece. The starting point of the algorithm is the stereolithography (STL) 3D model of the piece. The STL model can be easily generated by any CAD software, and it models each object as a set of triangles forming a polygonal mesh. Internally, the file stores a matrix $\mathbf{V} \in \mathbb{R}^{3 \times n_v}$ of n_v vertices in the space, and $\mathbf{F} \in \mathbb{N}^{3 \times n_f}$ that encodes the vertices association of the n_f faces constituting the polygonal mesh. As an example, for the planar mesh in Fig.1, the corresponding matrices \mathbf{V}, \mathbf{F} are given by:

$$\mathbf{V} = \begin{bmatrix} 0 & 3 & 6 & 5 & 2 \\ 0 & 0 & -1 & 2 & 2 \\ 0 & 0 & 0 & 0 & 0 \end{bmatrix}, \quad \mathbf{F} = \begin{bmatrix} 1 & 2 & 2 \\ 2 & 4 & 3 \\ 5 & 5 & 4 \end{bmatrix}, \quad (1)$$

where $V_i \in \mathbb{R}^3$ are the Euclidean coordinates of the i -th vertex, corresponding to the i -th column of \mathbf{V} , while the indexes of the vertices for the j -th face F_j are listed in the j -th column of \mathbf{F} . In the following, we denote by \mathcal{M} a mesh, which is defined by the vertices \mathbf{V} and the faces \mathbf{F} .

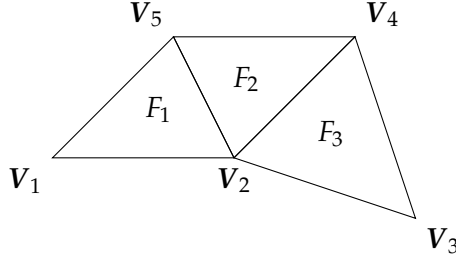


Figure 1: Example of polygonal mesh with $n_v = 5$ vertices and $n_f = 3$ faces.

2.2 Point clouds

Stereo cameras leverage the disparity map of 2 images taken at known relative positions to associate a depth value with each pixel, thus constructing a 3D representation of the scene, thus generating a point cloud. More in depth, given the k -th point cloud acquisition, a point cloud can be seen as a set \mathcal{Z}_k of n_p 3D points in the space described in the camera's reference frame $\langle C \rangle$:

$$\mathcal{Z}_k = \left\{ z_{k,i}^{(c)} \in \mathbb{R}^3, i = 1, \dots, n_p \right\}. \quad (2)$$

From a metrological perspective, each registered element of the point $z_{k,i}^{(c)}$ is a nonlinear function h^* (i.e., the sensor model) of the actual scene in view \mathcal{S} and of the camera pose $\mathbf{p}_c \in SE(3)$ (where $SE(3)$ is the special Euclidean group, that is $\mathbb{R}^3 \times SO(3) \subset \mathbb{R}^6$), with the addition of an uncertainty term $\varepsilon_{k,i} \in \mathbb{R}^3$ deriving from the camera and the reconstruction algorithm:

$$z_{k,i}^{(c)} = h^*(\mathcal{S}, \mathbf{p}_c) + \varepsilon_{k,i}. \quad (3)$$

An analytical derivation of $\varepsilon_{k,i}$ is very difficult since the uncertainties depend on the intrinsic and extrinsic parameters of the camera, on the parameters of the built-in point-cloud reconstruction algorithm and on the environmental conditions. To overcome this limitation, Ortiz et al. carried out in [20] a Type A statistical analysis on a commercial stereo-camera to reconstruct the root-mean-square error (RMSE) of each collected point. Based on this work and in light of the Central Limit Theorem, we assume $\varepsilon_{k,i} \sim \mathcal{N}(0, \mathbf{R}_{k,i})$ and white, that is normally distributed, with zero mean, and with a covariance matrix defined as

$$\mathbf{R}_{k,i}(\rho) = a e^{b\rho} \mathbf{I}_{3 \times 3}, \quad (4)$$

with $a, b \in \mathbb{R}$ coefficients that depend on the image acquisition resolution and $\rho \in \mathbb{R}^+$ the distance between the camera origin and the acquisition point.

2.3 Measurement model

To define the measurement model, we define a state that captures the dissimilarity between the inspected object and its reference shape resulting from the CAD model. We first notice that the scene in view \mathcal{S} in (3) corresponds to the mesh \mathcal{M} , except for the presence of the defects. Indeed, by the defining with \mathcal{S}_n the scene for a perfect nominal workpiece, the knowledge of \mathbf{p}_c (given by an external measurement system or by mounting the stereo camera on a robot end effector) allows us to write

$$h^{**}(\mathcal{M}) = h^*(\mathcal{S}_n, \mathbf{p}_c). \quad (5)$$

Notice that the uncertainties in the knowledge of \mathbf{p}_c are embedded in $\varepsilon_{k,i}$ in (3). To detect the defect, we are interested in determining the regions of the mesh \mathcal{M} in which the equation in (5) does not hold. To this end, for each measurement $z_{k,i}^{(c)}$ in (3), we first compute the point $\bar{z}_{k,i,j} \in \mathbb{R}^3$ obtained through a ray-cast with the mesh \mathcal{M} , i.e., $\bar{z}_{k,i,j} \in \mathcal{M}$ is the closest point to $z_{k,i}^{(c)}$ and belongs to the

face F_j of the mesh. Therefore, $\bar{z}_{k,i,j} = f(\mathbf{z}_{k,i}^{(c)})$. For the nominal scene \mathcal{S}_n and in the ideal case of no uncertainties, there exists $j \in \{1, \dots, n_f\}$ such that $\mathbf{z}_{k,i}^{(c)} = \bar{z}_{k,i,j}$. In the presence of defects but still in the ideal case of no uncertainties, we can model the difference using the dissimilarity measure $x_{k,i,j}$, i.e. $\mathbf{h}^*(\mathcal{S}, \mathbf{p}_c)$ in (3) becomes

$$\mathbf{h}^*(\mathcal{S}, \mathbf{p}_c) = \bar{z}_{k,i,j} + x_{k,i,j} \bar{\mathbf{n}}_j, \quad (6)$$

where $\bar{\mathbf{n}}_j$ is the normal direction of the j -th face, defined using \mathbf{V} and \mathbf{F} in (1). Hence, for each gathered point cloud, we have an indirect measurement of $x_{k,i,j}$ for the j -th face, thus leading to the following indirect measurement function

$$\delta_{k,i,j} = g(\mathbf{z}_{k,i}^{(c)}) = \mathbf{z}_{k,i}^{(c)} - \bar{z}_{k,i,j} = x_{k,i,j} \bar{\mathbf{n}}_j. \quad (7)$$

When the uncertainties $\varepsilon_{k,i}$ comes into play, we have $f(\mathbf{z}_{k,i}^{(c)}) = \bar{z}_{k,i,j} + \boldsymbol{\eta}_{k,i,j}$, where $\boldsymbol{\eta}_{k,i,j}$ is the effect of $\varepsilon_{k,i}$ through the ray tracing function. Therefore, (7) turns to

$$\delta_{k,i,j} = x_{k,i,j} \bar{\mathbf{n}}_j + \varepsilon_{k,i} + \boldsymbol{\eta}_{k,i,j} \approx x_{k,i,j} \bar{\mathbf{n}}_j + \varepsilon_{k,i}, \quad (8)$$

where we have assumed that, being $\boldsymbol{\eta}_{k,i,j}$ a function of $\varepsilon_{k,i}$ and using the actual mesh as reference, the effect of $\boldsymbol{\eta}_{k,i,j}$ is already embedded into $\varepsilon_{k,i}$. By noticing that all the cloud points falling on the face F_j are just multiple measurement of the same quantity $x_{k,i,j}$, we simply define the state to be estimated as $\mathbf{x}_k = [x_{k,1}, \dots, x_{k,n_f}]^\top \in \mathbb{R}^{n_f}$, which quantifies the deviation between the nominal model and the measurements: whenever a state component approaches zero, we expect a low discrepancy between the corresponding face of the two meshes. On the other hand, a high value of $|x_{k,i}|$ is reasonably associated with a high discrepancy and hence with the presence of a defect in the area.

2.4 Bayesian filtering

In order to build an estimator for the vector \mathbf{x}_k , we start with a weighted least squares solution. First, we define the vector of measurements (8) as

$$\Delta_k = \begin{bmatrix} \delta_{k,1,j_1}^\top & \delta_{k,2,j_2}^\top & \cdots & \delta_{k,n_p,j_{n_p}}^\top \end{bmatrix},$$

where j_l is the index of the face associated with the l -th measurement. Therefore

$$\Delta_k = \mathbf{H}_k \mathbf{x}_k,$$

where $\mathbf{H}_k \in \mathbb{R}^{3n_p \times 3n_f}$. In particular

$$\delta_{k,i,j_i}^\top = \mathbf{H}_k^{(i)} \mathbf{x}_k,$$

where the $3 \times 3n_f$ block $\mathbf{H}_k^{(i)}$ of \mathbf{H}_k pertaining to the i -th indirect measurement is a matrix of all zeros except for the j_i -th column, which is equal to $\bar{\mathbf{n}}_{j_i}$. Given (8), we can also immediately derive that the covariance matrix of the measurement uncertainties of Δ_k is given by

$$\mathbf{R}_k = \text{blkdiag} \left\{ \mathbf{R}_{k,i}(\|\mathbf{z}_{k,i}^{(c)}\|), i = 1, \dots, n_p \right\} \in \mathbb{R}^{3n_p \times 3n_p}, \quad (9)$$

where $\rho = \|\mathbf{z}_{k,i}^{(c)}\|$ in (4) has been used and where the point cloud uncertainties are approximated as uncorrelated in space. A more detailed analysis on this specific point is left for future works.

At the beginning of the algorithm, we initialise our estimates with two dummy values $\hat{\mathbf{x}}_0$ and \mathbf{P}_0 : $\hat{\mathbf{x}}_0$ is the first estimate of the actual $\mathbf{x}_k = \mathbf{x}$ (since the defects did not change along the point clouds collection); \mathbf{P}_0 is the rated covariance matrix of the estimation error $\mathbf{x} - \hat{\mathbf{x}}_0$. Then, a recursive weighted least-squares (RWLS) estimation algorithm, i.e., a Bayesian filter, can be applied, thus having for $k \geq 1$

$$\begin{aligned} \mathbf{S}_{k+1} &= \mathbf{H}_{k+1} \mathbf{P}_k \mathbf{H}_{k+1}^\top + \mathbf{R}_{k+1}, \\ \mathbf{W}_{k+1} &= \mathbf{P}_k \mathbf{H}_{k+1}^\top \mathbf{S}_{k+1}^{-1}, \\ \hat{\mathbf{x}}_{k+1} &= \hat{\mathbf{x}}_k + \mathbf{W}_{k+1} (\Delta_{k+1} - \mathbf{H}_{k+1} \hat{\mathbf{x}}_{k+1}), \\ \mathbf{P}_{k+1} &= (\mathbf{I} - \mathbf{W}_{k+1} \mathbf{H}_{k+1}) \mathbf{P}_k. \end{aligned} \quad (10)$$

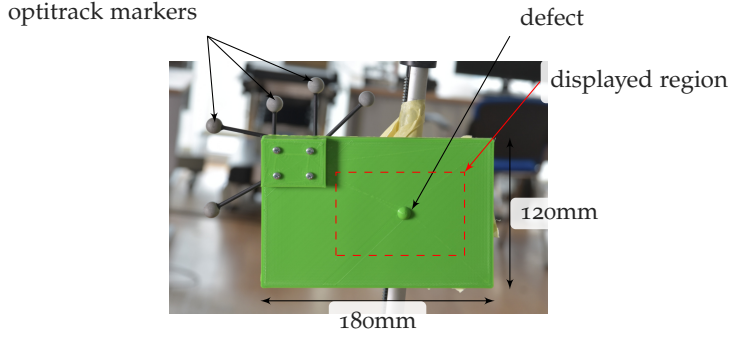


Figure 2: 3D printed tablet containing one defect in the middle of the board. The area bounded by the red line is the region that will be displayed in the following figures.

2.5 Information filter

From a numerical point of view, using a RWLS estimator might not be beneficial due to the high dimensionality of the problem. In fact, each point-cloud usually comprises tens of thousands of points, while the STL derived from a complex CAD might easily reach millions of faces. Since with the application of the RWLS we are implicitly considering that the state $x \sim \mathcal{N}(\hat{x}_k, \mathbf{P}_k)$ is drawn from a Gaussian distribution, we can reduce the numerical complexity resorting to the dual representation of (10) in the information domain. Let $\boldsymbol{\zeta}_k \in \mathbb{R}^{3n_f}$ and $\boldsymbol{\Omega}_k \in \mathbb{R}^{3n_f \times 3n_f}$ be respectively the information vector and matrix, given the transformation

$$\mathbf{P}_k = \boldsymbol{\Omega}_k^{-1} \text{ and } \hat{x}_k = \boldsymbol{\Omega}_k^{-1} \boldsymbol{\zeta}_k, \quad (11)$$

then (10) is mapped into

$$\begin{aligned} \boldsymbol{\Omega}_{k+1} &= \mathbf{H}_k^\top \mathbf{R}_k^{-1} \mathbf{H}_k + \boldsymbol{\Omega}_k \\ \boldsymbol{\zeta}_{k+1} &= \mathbf{H}_k^\top \mathbf{R}_k^{-1} \mathbf{z}_k + \boldsymbol{\zeta}_k. \end{aligned} \quad (12)$$

This algorithm requires less computation, thus increasing the computational efficiency. In addition, information representations are sparse, thus code can be optimised to reduce memory requirements and computational costs [21].

3 Experimental Analysis

To evaluate the proposed algorithm, we designed and 3D printed a flat tablet, shown in Fig. 2, presenting in the middle a unique spherical defect of radius 5 mm. Doing so, we have a ground truth to address the properties of the estimation algorithm. Instead, the performance of the detection algorithm have been computed considering the defect-free shape of the CAD, i.e., a flat rectangular surface. With this set-up, the algorithm can be tested against different polygonal densities of the mesh, so as to assess the perception performance of the system in different settings. In the following, the mesh size represents the minimum edge length of the right-angled equilateral triangle resulting from the meshing algorithm.

Measurements have been collected from 2 commercially available stereo cameras: the Intel RealSense D415, and the StereoLabs Zed2. Both cameras were used at the resolution 1280×720 px and, according to [20], we select in (4) $a = 0.0184$ and $b = 0.2106$. The RealSense camera is an active sensor, so, to reduce the uncertainty of the point-cloud computation, it exploits a projected infrared pattern on the environment. On the other hand, the Zed2 is a passive sensor, thus it requires a good illumination to improve the quality of the reconstructed point-cloud. For this reason, we illuminated the tablet sample with 2 soft-boxes photo lights.

To provide the camera pose p_c in (3), we used the OptiTrack motion capture system. Since the provided data were not of sufficient to match the CAD model with the registered point-clouds with

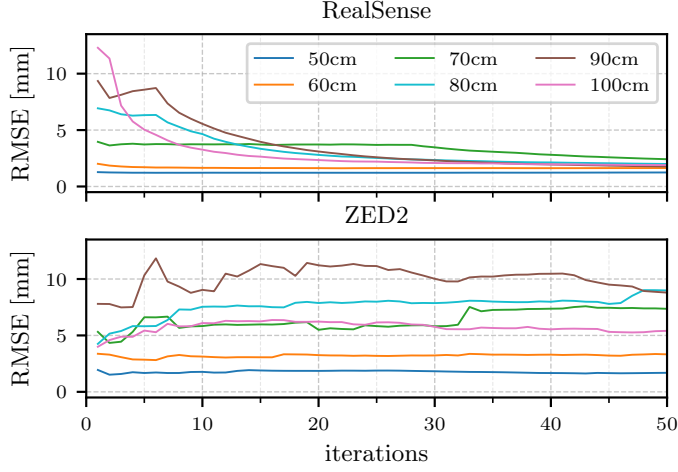


Figure 3: RMSE of the algorithm computed on a 5 mm as function of the iterations and relative distances between object and camera for the two compared devices.

millimetre precision, at each iteration the method calls an iterative closest point (ICP) algorithm to improve alignment of the measurement with the known CAD model. The algorithm has been implemented in C++, using ROS2 as middleware to communicate between cameras and the OptiTrack system.

3.1 Results

For each of the following tests, the algorithm is initialised with zero state $\hat{x}_0 = 0$ and a diagonal covariance $\mathbf{P}_0 = \sigma_0^2 \mathbf{I}$, with $\sigma_0 = 50$ mm. To evaluate the algorithm and compare the two camera systems, we use the RMSE defined as

$$\text{RMSE}(k) = \sqrt{\frac{1}{n_{f,v}} \mathbf{e}_k^\top \mathbf{e}_k}, \quad \mathbf{e}_k = (\hat{\mathbf{x}}_k - \mathbf{x}) \mathbf{\Pi}, \quad (13)$$

with $\hat{\mathbf{x}}_k$ the state estimate at the k -th iteration (i.e., when k point clouds are acquired), \mathbf{x} is the reference state that is obtained by geometrical difference between the CAD model of the defective and defect-free objects, and $(\pi_{ij}) = \mathbf{\Pi} \in \mathbb{R}^{n_f \times n_{f,v}}$, $\pi_{ij} \in \{0, 1\}$ is a matrix used to select the $n_{f,v}$ triangular faces involved in the measurements. In fact, only half of the tablet is directly visible from the camera, thus only those polygons can be updated. In addition, since our method relies on ray-casting to create correspondences with the mesh, areas close to the edges appear to be highly distorted, so all triangle within 6 mm from the border have been neglected in the performance metrics.

As first step, we compared the algorithm outcomes with the two cameras while inspecting the tablet at different distances, with the tablets normal pointing toward the camera. As shown in Fig. 3, it is possible to observe that the RealSense camera, even at different acquisition distances, converges to a RMSE slightly above the 2 mm mark. On the other hand, the Zed2 shows a trend for which, as distance increases, the RMSE increases as well.

To push forward the analysis, we report the distribution of the state estimation error on the testing tablet. As shown in Fig. 4, the state estimate provided by the RealSense camera is qualitatively better, appearing consistent with the reality, while the Zed2 present several issues. This is the case notwithstanding the different light conditions: irrespective of the adoption of natural environment illumination, positioning one soft-box on one side of the tablet, and positioning 2 soft-boxes at both sides, the estimates we obtained were comparable.

These results can be directly linked with the different camera working principles. Being the RealSense an active sensor, the projected light pattern on the tablet enables a more accurate and

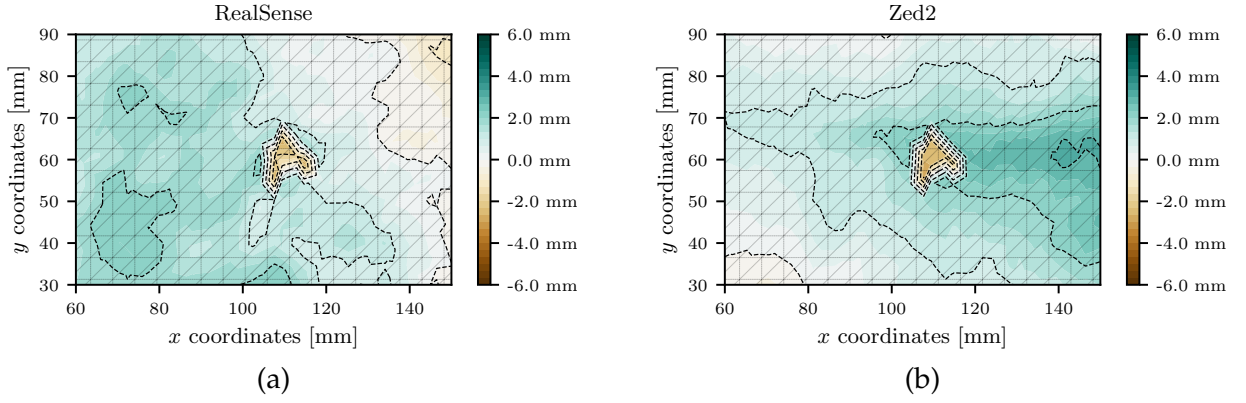


Figure 4: Estimation error $e_{50} = \hat{x}_{50} - x$, in the region of interest, for the Realsense (a) and Zed2 (b) cameras at the 50-th iteration. Measurements have been taken at 50 cm, and the mesh has size of 5 mm. Drawn isolines mark the barrier at each whole integer step of error. The reported triangular grid is the one of the mesh actually used to carry out the estimation.

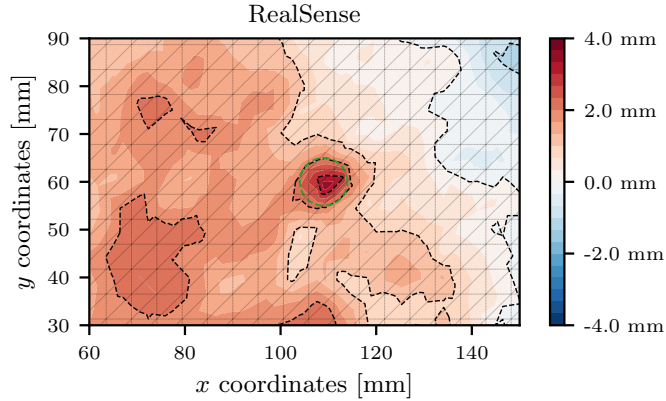


Figure 5: State estimate \hat{x}_{50} , in the region of interest, for the Realsense camera and location of the spherical defect (dashed green line). Experiment setup as in Fig. 4. The reported triangular grid is the one of the mesh actually used to carry out the estimation.

dense point-cloud reconstruction, while, at a relatively low distance from the object, the passive Zed2 camera struggles in the identification of the correspondences using the disparity map only. In numbers, each triangular face of the 5 mm mesh in the region of interest is sampled throughout the 50 iterations, on average, 2200 times using the RealSense, and 150 times using the Zed2. This is also reflected on the standard deviation of the estimated state that, for tests shown in Fig. 4, are respectively 0.25 mm and 0.95 mm for the RealSense and the Zed2.

By looking at Fig. 5, which depicts the state estimate obtained by collecting 50 measurements at a distance of 50 cm using the RealSense camera, it is clear that the system is able to capture the presence of the defect. Still, we must also note that outside of the region of interest, the state estimate appears diverging. Looking at different experimental outcomes, it emerges a pattern for which the central region of the tablet is overestimated, while peripheral areas are under-estimated. These errors can be associated to a non-correct calibration of the sensing devices. The measurement model indeed considers the uncertainties $\varepsilon_{k,i}$ to have zero means, i.e. the measurement has been compensated from any systematic error. Even though the measurement uncertainty covariance (4) proved to be effective in general, no model compensation is performed. It is indeed possible that, at the distances we tested the camera, optical reconstruction distortions can introduce a bias in the measurements. The deeper investigation of this issue is left for future developments.

After multiple tests, we concluded that best results are obtained at the minimum distance of

Table 1: Mean and standard deviation of the absolute error at the 50-th iteration of the algorithm as function the relative heading between camera orientation and the tablet normal. All acquisition took at a distance of 50 cm with mesh of 5 mm.

Angle	RealSense		Zed2	
	mean($ e_{50} $)	std($ e_{50} $)	mean($ e_{50} $)	std($ e_{50} $)
0°	1.02mm	0.73 mm	1.21mm	1.13mm
10°	0.84mm	0.54 mm	3.18mm	3.16mm
15°	0.84mm	0.62 mm	3.04mm	2.40mm
20°	0.80mm	0.63 mm	3.58mm	3.37mm
30°	0.95mm	0.79 mm	4.27mm	3.59mm
45°	0.83mm	0.82 mm	8.02mm	10.73mm
60°	1.04mm	1.09 mm	17.24mm	17.72mm
75°	1.49mm	1.52 mm	22.85mm	19.64mm

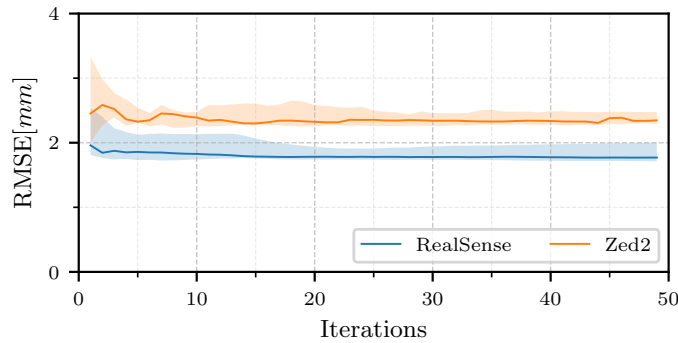


Figure 6: Median and quartiles of the RMSE distribution, as a function of the algorithm iterations, for the 2 cameras. For each camera, we performed 10 tests at a distance of 50 cm and zero relative heading. Tests carried out on mesh of size 5 mm.

50 cm, due to a lower measurement uncertainty given by the model (4), and a higher amount of casted rays on the mesh. At this distance, then we also analysed the impact of the relative orientation between the camera pointing direction and the tablet normal direction. As reported in Table 1, where the mean and the standard deviation of the absolute estimation error is reported, the RealSense camera confirms better performance in this situation as well. Within the 50° relative heading, the RealSense appears to work consistently to reality, and all tests clearly show the pattern associated to the non-correct compensation of the measurement bias. On the other hand, Zed2 camera results get worse as the heading increases.

Finally, to assess the repeatability of the algorithm, we performed multiple trials with fixed experimental conditions. In this case, as depicted in Fig. 6, tests carried out with the RealSense camera shows a convincing convergence patterns. After about 30 iterations, the RMSE for the RealSense converges to a characteristic value that can be related both to acquisition distance and relative heading. On the other hand, the algorithm executed on the Zed2 camera has an inconsistent behavior, highlighting how the sensor does not provide satisfactory results both in terms of accuracy and repeatability.

One final, yet remarkable note, consists in the choice of the CAD mesh size. By construction, the state represent the normal deviation averaged on each triangle, thus to have a good spatial resolution, smaller polygons are requested. This, in turn, increases the number n_f of faces that, at some point, will make the RWLS algorithm (10), even in it's information representation (12), unsolvable in reasonable time. In all these tests, we found that the 5 mm mesh was the best compromise in terms of spatial resolution, and computational time, with point-cloud processing requiring 10 s per algorithm iteration. In practice, this solution as is, can't be used in a online system due to the com-

putational burden. However it is also true that, for the sake of simplicity, code has been developed using a sequential approach, but the algorithm formulation is heavily parallelisable on dedicated hardware, so with ad-hoc implementation we expect a drastic reduction of processing time.

4 Conclusions

In this work, we evaluated the use of the CAD knowledge of a workpiece within a RWLS to incrementally estimate surface defects using commercially available stereo-cameras. Within the proposed approach, the estimator converges to a standard deviation of 0.3 mm in approximately 40 s, i.e., in 1 s of point-cloud acquisitions. While we acknowledge the limitations of the approach, potential solutions are within reach. Calibration issues can be addressed through bias modelling techniques. To overcome computational limitations, the algorithm can be parallelised for more efficient processing on modern hardware. Furthermore, the current implementation focuses on static measurements. Exploiting the motion provided by robotic manipulators, future works will investigate planning strategies to optimise information gathering based on the specific workpiece geometry and potential defect types. This will allow for a more targeted and efficient inspection process. Overall, the proposed method paves the way for utilising commercially available stereo cameras for high-precision quality control applications. By leveraging CAD models and addressing the identified limitations, this approach has the potential to become a robust and cost-effective solution for automated surface defect detection in various manufacturing and inspection scenarios.

ACKNOWLEDGEMENTS

Co-funded by the European Union. Views and opinions expressed are however those of the author(s) only and do not necessarily reflect those of the European Union or the European Commission. Neither the European Union nor the granting authority can be held responsible for them. EU - HE Magician – Grant Agreement 101120731.

References

- [1] S. Catalucci, A. Thompson, S. Piano, D. T. Branson, and R. Leach, "Optical metrology for digital manufacturing: a review," *The International Journal of Advanced Manufacturing Technology*, vol. 120, no. 7–8, p. 4271–4290, Apr. 2022.
- [2] A. Andersson, "Evaluation and visualisation of surface defects on auto-body panels," *Journal of Materials Processing Technology*, vol. 209, no. 2, pp. 821–837, 2009.
- [3] J. Salcedo-Hernández, J. García-Barruetabeña, I. Pastor-López, and B. Sanz-Urquijo, "Predicting enamel layer defects in an automotive paint shop," *IEEE Access*, vol. 8, pp. 22 748–22 757, 2020.
- [4] L. Arnal, J. E. Solanes, J. Molina, and J. Tornero, "Detecting dings and dents on specular car body surfaces based on optical flow," *Journal of Manufacturing Systems*, vol. 45, pp. 306–321, 2017.
- [5] J. Molina, J. E. Solanes, L. Arnal, and J. Tornero, "On the detection of defects on specular car body surfaces," *Robotics and Computer-Integrated Manufacturing*, vol. 48, pp. 263–278, 2017.
- [6] Q. Zhou, R. Chen, B. Huang, W. Xu, and J. Yu, "Deepinspection: Deep learning based hierarchical network for specular surface inspection," *Measurement*, vol. 160, p. 107834, 2020.
- [7] Z. Sárosi, W. Knapp, A. Kunz, and K. Wegener, "Detection of surface defects on sheet metal parts by using one-shot deflectometry in the infrared range," in *Infrared Camera Applications Conference 2010*. ETH Zurich, IWF, 2010, pp. 243–254.

- [8] Q. Zhou, R. Chen, B. Huang, C. Liu, J. Yu, and X. Yu, "An automatic surface defect inspection system for automobiles using machine vision methods," *Sensors*, vol. 19, no. 3, 2019.
- [9] F. Xie, R. Chen, Q. Zhou, Y. Zhao, and T. Sui, "An adaptive defect detection technology for car-bodies surfaces," in *2019 Chinese Automation Congress (CAC)*, 2019, pp. 1023–1028.
- [10] J. Zhang, J. Xu, L. Zhu, K. Zhang, T. Liu, D. Wang, and X. Wang, "An improved mobilenet-ssd algorithm for automatic defect detection on vehicle body paint," *Multimedia Tools and Applications*, vol. 79, no. 31–32, pp. 23 367–23 385, Jun. 2020.
- [11] F. Chang, M. Dong, M. Liu, L. Wang, and Y. Duan, "A lightweight appearance quality assessment system based on parallel deep learning for painted car body," *IEEE Transactions on Instrumentation and Measurement*, vol. 69, no. 8, pp. 5298–5307, 2020.
- [12] Y. Gao, L. Gao, X. Li, and X. V. Wang, "A multilevel information fusion-based deep learning method for vision-based defect recognition," *IEEE Transactions on Instrumentation and Measurement*, vol. 69, no. 7, pp. 3980–3991, 2020.
- [13] D. Maestro-Watson, J. Balzategui, L. Eciolaza, and N. Arana-Arexolaleiba, "Deflectometric data segmentation for surface inspection: a fully convolutional neural network approach," *Journal of Electronic Imaging*, vol. 29, no. 4, p. 041007, 2020.
- [14] S. B. Block, R. D. da Silva, L. B. Dorini, and R. Minetto, "Inspection of imprint defects in stamped metal surfaces using deep learning and tracking," *IEEE Transactions on Industrial Electronics*, vol. 68, no. 5, pp. 4498–4507, 2021.
- [15] Y. Zhao, Q. Liu, H. Su, J. Zhang, H. Ma, W. Zou, and S. Liu, "Attention-based multiscale feature fusion for efficient surface defect detection," *IEEE Transactions on Instrumentation and Measurement*, vol. 73, pp. 1–10, 2024.
- [16] J. Lehr, J. Philipps, V. N. Hoang, D. v. Wrangel, and J. Krüger, "Supervised learning vs. unsupervised learning: A comparison for optical inspection applications in quality control," *IOP Conference Series: Materials Science and Engineering*, vol. 1140, no. 1, p. 012049, May 2021.
- [17] M. Germani, F. Mandorli, M. Mengoni, and R. Raffaelli, "Cad-based environment to bridge the gap between product design and tolerance control," *Precision Engineering*, vol. 34, no. 1, pp. 7–15, 2010, CIRP-CAT 2007.
- [18] M. Sjö Dahl, P. Bergström, M. Fergusson, K. Söderholm, and A. Andersson, "In-line quality control utilizing close-range photogrammetry and a cad-model," *Engineering Research Express*, vol. 3, no. 3, p. 035029, aug 2021.
- [19] C. Long, C. Fang, Z. Li, Y. Jiang, and L. Duan, "Reconstruction of 3-d cad model of work-piece with internal defect based on industry ct image," *IEEE Transactions on Instrumentation and Measurement*, vol. 72, pp. 1–11, 2023.
- [20] L. Ortiz, E. Cabrera, and L. Gonçalves, "Depth data error modeling of the zed 3d vision sensor from stereolabs," *Electronic Letters on Computer Vision and Image Analysis*, vol. 17, 04 2018.
- [21] S. Thrun, W. Burgard, and D. Fox, *Probabilistic robotics.*, ser. Intelligent robotics and autonomous agents. MIT Press, 2005.